

PACS numbers: 42.30.Wb; 87.64.Cc
DOI: 10.1070/QE2008v038n06ABEH013834

Algebraic reconstruction and postprocessing in one-step diffuse optical tomography

A.B. Konovalov, V.V. Vlasov, D.V. Mogilenskikh, O.V. Kravtsenyuk, V.V. Lyubimov

Abstract. **The photon average trajectory method is considered, which is used as an approximate method of diffuse optical tomography and is based on the solution of the Radon-like trajectory integral equation. A system of linear algebraic equations describing a discrete model of object reconstruction is once inverted by using a modified multiplicative algebraic technique. The blurring of diffusion tomograms is eliminated by using space-varying restoration and methods of nonlinear colour interpretation of data. The optical models of the breast tissue in the form of rectangular scattering objects with circular absorbing inhomogeneities are reconstructed within the framework of the numerical experiment from optical projections simulated for time-domain measurement technique. It is shown that the quality of diffusion tomograms reconstructed by this method is close to that of tomograms reconstructed by using Newton-like multistep algorithms, while the computational time is much shorter.**

Keywords: *diffuse optical tomography, photon average trajectory, algebraic reconstruction. space-varying restoration, nonlinear colour palette.*

1. Introduction

Diffuse optical tomography (DOT) [1 – 3] is a promising method for biomedical visualisation allowing probing of optically thick (8 – 10 cm) tissues in the so-called therapeutic transparency window in the near-IR range from 700 to 900 nm. This method involves position-dependent measurements when signals from several laser radiation sources are observed with several photodetectors. Information on spatially localised properties of tissues is obtained by solving the inverse problem, i.e. the tomographic reconstruction problem. Diffuse optical tomography is a noninvasive, harmless, and relatively low-cost method of biomedical visualisation. It is very important that DOT allows the visualisation of spatial distributions of functional parameters (the degree of oxygenation of the blood haemoglobin, concentration of various cytochromes such as bilirubin, melanin, cytochrome oxidase, etc.) and, hence, is quite promising for early and efficient diagnostics of oncology diseases [1, 4]. The main disadvantage of DOT is its low spatial resolution due to multiple scattering of photons, which have no regular trajectories and are distributed over the entire volume V under study. As a result, each point in the volume makes a significant contribution to the detected signal. In the case of time-domain measurement technique, the inverse DOT problem in the approximation of the small perturbation theory of Born or Rytov is reduced to the solution of the integral equation [5 – 7]

$$g(t) = \int_V \left\{ \int_0^t (c/n) P[\boldsymbol{r}, \tau | (\boldsymbol{r}_\mathrm{s}, 0) \to (\boldsymbol{r}_\mathrm{d}, t)] \mathrm{d}\tau \right\} \delta\mu_\mathrm{a}(\boldsymbol{r}) \mathrm{d}^3 r, \quad (1)$$

where $g(t)$ is the optical projection of absorbing inhomogeneities (relative change in the optical signal caused by inhomogeneities) measured for the detector delay time t; c/n is the speed of light in the medium; $P[\boldsymbol{r}, \tau | (\boldsymbol{r}_\mathrm{s}, 0) \to (\boldsymbol{r}_\mathrm{d}, t)]$ is the density of the conditional probability that a photon moving from a spatiotemporal point $(\boldsymbol{r}_\mathrm{s}, 0)$ of a source to a spatiotemporal point $(\boldsymbol{r}_\mathrm{d}, t)$ of a detector reaches an intermediate point $\boldsymbol{r}$ for the time τ; and $\delta\mu_\mathrm{a}(\boldsymbol{r})$ is the function describing the distribution of absorbing inhomogeneities (object function). An integral equation written in form (1) is usually inverted with the help of multistep Newton-like reconstruction techniques based on the variational formulation of the radiation transfer equation (or its diffusion approximation) [1, 2]. These algorithms provide a comparatively high spatial resolution (~ 0.5 cm) for diffusion tomograms, but they are not fast enough for real-time diagnostics because the problem of propagation of radiation through a medium is solved numerically at each step of the iteration process.

Lyubimov et al. [5 – 7] have shown that the reconstruction can be considerably accelerated by replacing integration over the volume in (1) by integration over a conditional trajectory connecting a point source with a point detector. By using the probability interpretation of radiation transfer with the conditional probability density P, integral (1) can be written in the form

A.B. Konovalov, V.V. Vlasov, D.V. Mogilenskikh Russian Federal Nuclear Center, E.I. Zababakhin All-Russian Research Institute of Technical Physics, P.O. Box 245, 456770 Snezhinsk, Chelyabinsk region, Russia; e-mail: a_konov@mail.vega-int.ru, valsovvv-1981@yandex.ru, d.v.mogilensskikh@vniif.ru;
O.V. Kravtsenyuk Institute of Electronic Structure & Lasers, Foundation for Research and Technology – Hellas, P.O. Box 1527, Vassilika Vouton, 71110 Heraklion, Crete, Greece; e-mail: olgakr@iesl.fort.gr;
V.V. Lyubimov S.I. Vavilov State Optical Institute, Scientific and Industrial Corporation, Birzhevaya liniya 12, 1998034 St. Petersburg, Russia; e-mail: vv_lyubimov@mail.ru

Received 6 February 2008
Kvantovaya Elektronika **38** (6) 588 – 596 (2008)
Translated by M.N. Sapozhnikov

$$g(t) = \int_L \frac{\langle \delta\mu_a(\boldsymbol{r}) \rangle_P}{v(l)}\, \mathrm{d}l, \tag{2}$$

where L is the photon average trajectory (PAT); l is the distance along the PAT; $v(l)$ is the relative average velocity of photons moving along the PAT as a function of l; and $\langle \cdot \rangle_P$ is the operator of averaging over the spatial distribution of P. Integral equation (2) is an analogue of the Radon transform and can be inverted by using fast algorithms of X-ray tomography. In other words, the replacement of volume integral (1) by trajectory integral (2) allows us to pass from the multistep reconstruction to one-step reconstruction, i.e. the system of algebraic equations describing the discrete reconstruction model will be inverted only once. This one-step method, which is called the photon average trajectory (PAT) method [5], considerably reduces the computational time. However, integration over the trajectory in (2) is applied not to the object function $\delta\mu_a(\boldsymbol{r})$ itself but to the function averaged over the spatial distribution P. This means that, by inverting equation (2), only diffusion tomograms blurred after averaging can be directly reconstructed. To compensate for this *a priori* blurring, tomograms should be additionally processed.

In this paper, the PAT method is realised by using a multiplicative algebraic reconstruction technique (MART) for a planar layer geometry conventionally used in diffuse optical mammotomography [8–11]. We modified original Gordon formulas [12] for the solution correction to improve the convergence of the iteration reconstruction process and the quality of diffusion tomograms. Postprocessing was performed in two stages. At the first stage, the space-varying restoration was performed, which was based on the blurring model [13] adapted to the case of optical images [14]. At the second stage, we used the methods of nonlinear colour interpretation of data [15], which were developed at the Russian Federal Nuclear Center to increase the information content of images of gas-dynamic plasma objects. These methods are based on the formation of nonlinear analytic and statistical functions of correspondence between the image intensity and colour space, which allows the improvement of optical inhomogeneity profiles after algebraic reconstruction and space-varying restoration. The efficiency of the proposed realisation of the PAT method was estimated in a numerical experiment in which rectangular scattering objects with circular absorbing inhomogeneities simulating a pressed breast tissue with tumour structures were reconstructed from optical projections. The projections were simulated by solving the nonstationary diffusion equation with an instant point radiation source (the case of time-domain measurement technique). The limiting spatial resolution of the method was estimated quantitatively by using the modulation transfer function (MTF). We also studied the possibility of recognition of optical inhomogeneities simulating a tumour against the background of a random scattering medium, which is a healthy breast tissue containing fatty and parenchyma components. It is shown that the method proposed in the paper, which involves the reconstruction and postprocessing, provides a spatial resolution of ~ 0.6 cm along with a considerable computational time saving compared to multistep reconstruction techniques.

2. Algebraic reconstruction of diffusion tomograms

2.1 Formulation of the problem

Unlike the Radon transform, integration in (2) is performed along a curve L rather than along a straight line. Moreover, the weight distribution $1/v(l)$ in the integrand depends on spatial coordinates. Thus, to invert Eqn (2), it is necessary to calculate preliminarily the functions L and $v(l)$. It was shown in [5] that this can be performed by using the diffusion approximation of the transfer equation. If the photon density $\varphi(\boldsymbol{r}, \tau)$ satisfies the nonstationary diffusion equation for an instant point source and the Robin boundary condition [16], the probability density P is

$$P[\boldsymbol{r}, \tau | (\boldsymbol{r}_s, 0) \to (\boldsymbol{r}_d, t)] = \frac{\varphi(\boldsymbol{r}, \tau) G(\boldsymbol{r}_d - \boldsymbol{r}, t - \tau)}{\varphi(\boldsymbol{r}_d, t)}, \tag{3}$$

where $G(\boldsymbol{r}, \tau)$ is the Green function. The photon average trajectory, i.e. the trajectory of the mass centre of the photon distribution is described by the first statistical moment

$$\boldsymbol{R}(\tau) = \int_V \boldsymbol{r} P[\boldsymbol{r}, \tau | (\boldsymbol{r}_s, 0) \to (\boldsymbol{r}_d, t)] \mathrm{d}^3 r. \tag{4}$$

Correspondingly, the relative average photon velocity, i.e. the relative velocity of the mass centre of the distribution P is defined as the derivative

$$v(l) = \frac{n}{c} \left| \frac{\mathrm{d}\boldsymbol{R}}{\mathrm{d}\tau} \right|. \tag{5}$$

Analytic expressions for $\varphi(\boldsymbol{r}, \tau)$ and $G(\boldsymbol{r}, \tau)$ in the case of a homogeneous planar layer were analysed in detail in [17]. We used the results of this paper for numerical calculations of functions P, L and $v(l)$ from expressions (3), (4), and (5), respectively. Figure 1 presents the geometry of data recording that we used in simulations. The size of a rectangular scattering object is 11×8 cm. Triangles denote radiation sources on the object boundary, and circles indicate photodetectors. As an example, Fig. 1 shows four PATs and four corresponding banana-like bands (shown by grey), which we used for calculating the weight matrix (see below). Calculations were performed for the delay time

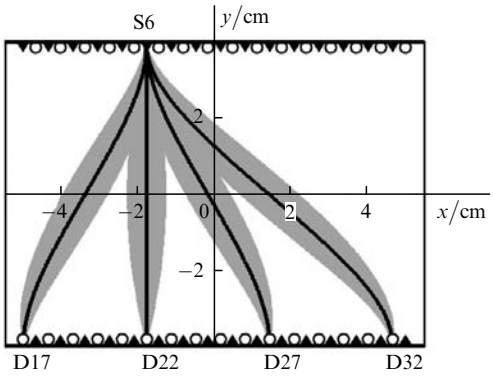

Figure 1. Data recording geometry in a numerical experiment. Triangles are radiation sources, circles are detectors.

3000 ps, the diffusion coefficient 0.034 cm, and the speed of light in the medium 0.0214 cm ps^{-1}. The coordinates of the indicated radiation sources and detectors were (in cm): S6 – (−1.77, 4), D17 – (−5, −4), D22 – (−1.77, −4), D27 – (−1.45, −4), D32 – (4.68, −4). We studied the transmission regime, and therefore only the connections between sources and detectors located on the opposite boundaries of the object were considered. Thus, a total number of average trajectories was 32×16 (32 sources and 16 detectors).

It is well known that integral equations like (2) can be solved by two fundamentally different methods. The first method is based on the analytic solution and the use of obtained inversion formulas to find the object function at discrete spatial points. The second method involves the representation of the integral equation in the form of a system of linear algebraic equations and its solution for a set of variables determining the discrete values of the object function. In our case, it is difficult to realise the first approach due to the PAT curvature. Our attempts to use the integral transformation algorithms for the reconstruction of diffusion tomograms [6, 14, 18] are based on the assumption that PATs are close to straight lines inside a scattering object. However, such an approach cannot be used for reconstructing accurately optical inhomogeneities near boundaries where PATs are strongly bended due to the avalanche-like migration of photons outside the object. Unlike integral methods, algebraic reconstruction methods based on the expansion into a series can be successfully used for bended trajectories and, hence, are preferable in this case.

Our experience of the algebraic reconstruction [19–21] shows that it is expedient to use a finite-width band instead of an infinitely narrow trajectory. This improves the convergence of the iteration process and increases the reconstruction accuracy. The configuration and size of the corresponding band should be chosen taking into account the spatial distribution of the trajectories of photons migrating from a point $(\boldsymbol{r}_s, 0)$ to a point $(\boldsymbol{r}_d, t)$. According to the statistical model considered above, the most probable trajectories are distributed in the region determined by the standard mean-square deviation (MSD) from the PAT described by the expression

$$\Delta(\tau) = \left\{ \int_V |\boldsymbol{r} - \boldsymbol{R}(\tau)|^2 P[\boldsymbol{r}, \tau | (\boldsymbol{r}_s, 0) \to (\boldsymbol{r}_d, t)] \mathrm{d}^3 r \right\}^{1/2}. \quad (6)$$

This region has the form of a banana [5] with apexes at the positions of sources and detectors on the boundary of a scattering object. Therefore, we use a band trajectory in the form of a banana-like band with a width directly proportional to the MSD: $\varepsilon(\tau) = \gamma\Delta(\tau)$. This means that, along with the probability density P, the first statistical moment $\boldsymbol{R}(\tau)$ (or L) and its derivative $v(l)$, it is also necessary to calculate the second moment $\Delta(\tau)$ before the reconstruction.

2.2 Discrete reconstruction model

The generalised 2-D reconstruction model is formulated as usual [5, 12, 19–21]. Let us introduce the Cartesian grid of square image elements covering an object. Let us assume that the function $\langle \delta\mu_a(\boldsymbol{r}) \rangle_P$ being reconstructed takes a constant value f_{kl} inside an element with indices k and l (hereafter, the (k, l) cell]. Let L_{ij} be the PAT connecting the ith source and the jth detector, and g_{ij} be the optical projection from the ith source measured with the jth detector. Then, a discrete reconstruction model can be described by the system of linear algebraic equations

$$g_{ij} = \sum_{k,l} W_{ijkl} f_{kl}, \quad (7)$$

where W_{ijkl} is the weighted contribution introduced by the (k, l) cell to the measured value of g_{ij} [hereafter, the (k, l) cell weight]. The weighted contribution is calculated from the expression

$$W_{ijkl} = \frac{S_{ijkl}}{v_{ijkl}\delta}, \quad (8)$$

where S_{ijkl} is the area of intersection of the band corresponding to the ith source and the jth detector [hereafter, the (i, j) band] with the (k, l) cell (Fig. 2); v_{ijkl} is the discrete relative velocity of the mass centre of the distribution P for the (i, j) band and (k, l) cell; and δ is the linear size of the cell. The boundaries of banana-like bands are determined by piecewise linear functions as follows.

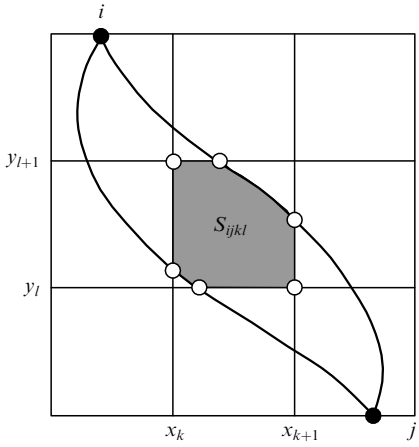

Figure 2. To the calculation of cell weights W_{ijkl}. The intersection of the (i, j) band with the (k, l) cell is shown.

(i) The sequence of discrete time moments $\{\tau_p\}$ is specified.

(ii) Perpendiculars to tangents at the PAT points corresponding to time moments $\{\tau_p\}$ are constructed (Fig. 3).

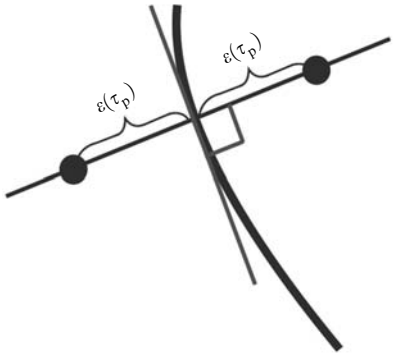

Figure 3. Scheme for determining the boundaries of a banana-like band on a two-dimensional grid.

(iii) Intervals of length $\varepsilon(\tau_p) = \gamma\Delta(\tau_p)$ are plotted in both directions along each perpendicular. The coefficient $\gamma \in (0, 1)$ is selected according to the condition that all the bands should fill the object region as much as possible. In our case, $\gamma = 0.25$.

(iv) Points obtained for different $\{\tau_p\}$ are connected by straight lines.

The areas $\{S_{ijkl}\}$ are found by determining points in which the boundaries of the bands intersect the cell boundaries. A polygon with apexes at these points and cell nodes is treated as the intersection of the (i, j) band and the (k, l) cell (Fig. 2). The set of discrete relative photon velocities v_{ijkl} is determined by using the algorithm described in detail in [20, 21].

2.3 Modified MART

The multiplicative algebraic reconstruction technique realising the method of entropy maximum is based on the iteration correction of the initial approximation $\{f_{kl}^{(0)}\}$. In each $(s + 1)$ iteration, the trajectories (bands) from only one source are considered. Thus, the correction is introduced to the approximation elements $\{f_{kl}^{(s)}\}$ corresponding to cells intersected by the given bands. In going from one iteration to another, sources are looked over cyclically. The Gordon formula of the introduction of correction to the sth approximation has the form [12]

$$f_{kl}^{(s+1)} = f_{kl}^{(s)} \left(g_{ij} \Big/ \sum_{k,l} W_{ijkl} f_{kl}^{(s)} \right)^{\lambda W_{ijkl}/\delta}, \tag{9}$$

where $\lambda \in (0, 1)$ is the parameter controlling the convergence rate of the iteration process. Expression (9) ignores the nonuniform distributions of the sum of weights and the number of solution corrections over cells. As a result, the MART often converges to an incorrect solution in the case of the insufficient amount of data, when system (7) proves to be strongly underdetermined. Due to the incorrect intensity redistribution, tomograms contain pronounced artefacts, often in regions where structures are absent in fact. To compensate for this disadvantage, we will use the following expression for the modified MART:

Step 1:

$$f_{kl}^{(s+1)} = f_{kl}^{(s)} \left(g_{ij} \Big/ \sum_{k,l} W_{ijkl} f_{kl}^{(s)} \right)^{\lambda W_{ijkl}/\tilde{W}_{kl}}, \tag{10}$$

where $\tilde{W}_{kl} = \sum_{i,j} W_{ijkl}/N_L$ is the reduced sum of weights for the (k, l) cell and N_L is a total number of bands used in the reconstruction.

Step 2:

$$f_{kl}^{(s+1)} = \frac{1}{(2q+1)^2} \sum_{m=-r}^{r} \sum_{n=-r}^{r} f_{k+m,l+n}^{(s+1)} \times \mathrm{norm}(\tilde{W}_{k+m,l+n}) \mathrm{norm}(A_{k+m,l+n}), \tag{11}$$

where an integer q specifies the size $q \times q$ of a smoothing window; A_{kl} is the number of solution corrections corresponding to the (k, l) cell; and

$$\mathrm{norm}(\xi_{kl}) = \left[\xi_{kl} - \min_{k,l}(\xi_{kl}) \right] \Big/ \left[\max_{k,l}(\xi_{kl}) - \min_{k,l}(\xi_{kl}) \right] \tag{12}$$

is the normalisation operator for distributions $\{\tilde{W}_{kl}\}$ and $\{A_{kl}\}$.

3. Postprocessing of diffusion tomograms

3.1 Space-varying restoration

By choosing the blurring model suitable for the restoration of the object function $\delta\mu_a(\boldsymbol{r})$, it is necessary to remember that the visualisation system like a diffuse optical tomograph is not invariant with respect to a spatial displacement. A strong dependence of the reconstruction accuracy on the position of an optical inhomogeneity being reconstructed follows directly from expression (6), which characterises the theoretical limit of the spatial resolution tending to zero near the object boundary. The resolution is the worst at the image centre and is determined by the object size. Thus, only the space-varying blurring model can be used for the restoration of diffusion tomograms.

The traditional approach [22] to the restoration of images subjected to space-varying blurring is based on the assumption that the invariance to displacements is preserved in local regions of the image. Each such region is restored with the help of its own spatially invariant point spread function (PSF) and then the results are sewed together to obtain the total real image. Such an approach produces artefacts at the boundaries of the joining, which should be then somehow eliminated. In this paper, we use the blurring model [13]. We used this model for the restoration of PAT tomograms [14] and also for compensation of the double-source effect in the X-pinch radiography [23]. According to this model, an image is divided into many regions where PSFs are approximately spatially invariant. However, instead of the restoration of each region separately and then combining the results, individual invariant PSFs are interpolated and the entire image is restored. The discrete restoration problem for PAT tomograms $\boldsymbol{f}$ with blurring is described by the system of linear algebraic equations

$$\boldsymbol{f} = \boldsymbol{Q}\boldsymbol{z}, \tag{13}$$

where $\boldsymbol{Q}$ is a large ill-conditioned matrix describing the blurring operator $\langle\cdot\rangle_P$ and $\boldsymbol{z}$ is the discrete representation of the real image $\delta\mu_a(\boldsymbol{r})$. The matrix $\boldsymbol{Q}$ contains nonzero elements of each of the spatially invariant PSFs corresponding to individual regions of a tomogram and also takes into account *a priori* information on the type of extrapolation of the image being restored outside its dimensions, i.e. the boundary conditions. This is necessary to compensate for artefacts near boundaries caused by the Gibbs effect. Thus, for example, in the case of reflective boundary conditions, which we use in the restoration, $\boldsymbol{Q}$ is a sum of the extended block Toeplitz matrix with extended Toeplitz blocks [24] and the extended block Hankel matrix with extended Hankel blocks [25].

Each spatially invariant PSF corresponding to an individual region of a diffusion tomogram was simulated by performing the following operations.

(i) On a triangle grid a point inhomogeneity is specified with the help of three equal values in the nodes of a triangle located in the centre of the region. The inhomogeneity amplitude exceeds the amplitude $\delta\mu_a(\boldsymbol{r})$ by an order of magnitude.

(ii) The point projections of the optical inhomogeneity are simulated by solving the nonstationary diffusion equation by the finite element method.

(iii) The PAT tomogram with the PSF is reconstructed by model optical projections with the help of the modified MART described above.

System (13) was inverted by using the iteration steepest descent algorithm [26], which converges rapidly enough and has the quasi-divergence with respect to the relative error $||\boldsymbol{z}_s - \boldsymbol{z}||/||\boldsymbol{z}||$, where $\boldsymbol{z}_s$ is the solution approximation at the sth iteration. This is very important for obtaining a regularised solution. In this paper, we omit details of realisation of the restoration algorithm of PAT tomograms. They are presented in [14].

3.2 Postprocessing by using a nonlinear colour palette

To improve the profiles of tomograms after the space-varying restoration, we used the methods of nonlinear colour interpretation of data [15]. These methods are based on the formation of nonlinear analytic and statistical functions of correspondence between the image intensity (values of the reconstructed object function) and palette colours [hereafter, the correspondence function (CF)]. A palette represents an ordered set of colours from the colour space where each colour is denoted by an ordinal number. If a palette is linear, the set of colours forms a linear trajectory in the colour space, while a nonlinear palette gives a curvilinear trajectory. Analytic CFs provide the correspondence between the image intensity and a colour in a cell by using nonlinear colour coordinate scales. For this purpose, elementary functions and their algebraic combinations are used. The choice of one or another combination depends on the operator and is performed based on *a priori* information contained in reconstructed and restored tomograms. Nonlinear statistical CFs are constructed by using statistical information on the distribution of colours of an initially chosen palette (as a rule, linear) among image cells. We realised an algorithm, which can be briefly described by the following sequence of steps.

(i) A linear CF is formed, i.e. the colour $C(z_{kl})$ of the chosen colour palette is assigned to the intensity z_{kl} in the (k, l) cell.

(ii) The number $N_C^{\text{cells}}(z_{kl})$ of cells of each colour in the palette is calculated and the weight vector W_C is determined, whose length is equal to the number of colours in the palette:

$$W_C(z_{kl}) = N_{\text{col}}\text{norm}\left[\frac{N_C^{\text{cells}}(z_{kl}) + 1}{N^{\text{cells}}}\right], \tag{14}$$

where N_{col} is the number of colours in the palette; N^{cells} is a total number of image cells; and $\text{norm}(\cdot)$ is the normalisation operator (12).

(iii) Based on the obtained statistical information, a statistical CF is calculated in the form of a spline approximation. In our case, the first-order spline is used:

$$C^{\text{stat}}(z_{kl}) = [C(z_{kl}) - N_{\text{col}}\text{norm}(z_{kl})]\times$$
$$\times[W_C(z_{kl}) - W_{C+1}(z_{kl})] + W_C(z_{kl}). \tag{15}$$

(iv) By summing statistical CF (15) and the initial linear CF, a nonlinear CF is formed.

Our experience [21] shows that the best result for the correction of profiles of reconstructed and restored optical inhomogeneities gives a combination of nonlinear analytic and statistical CFs.

4. Numerical experiment

4.1 Organisation of the experiment

To demonstrate the possibilities of the PAT method, we carried out the numerical experiment with scattering rectangular objects of size 11×8 cm (Fig. 1) simulating a pressed breast tissue, calculated optical projections and performed the reconstruction and postprocessing procedures described in sections 2 and 3. Calculations were performed for five objects. To estimate the limiting spatial resolution of the method, we used four objects, each of them containing two circular absorbing inhomogeneities of the same diameter simulating tumour structures. Inhomogeneities were located near centres of objects and were separated from each other by a diameter. The diameters of inhomogeneities of the four objects were 1.2, 1.0, 0.8, and 0.6 cm. The random structure of a healthy breast tissue was simulated by the method close to that used in [27] by specifying zigzag inclusions (parenchyma) against the background of a homogenous tissue (fat). In [27], the parenchymatous component was synthesised by the segmentation of a magnetic-resonance tomogram of a breast obtained in a clinic. We used the theory of cellular automats for this purpose [28]. Cellular automats are commonly used to construct alternative discrete models for simulation of physical process [29], when the application of traditional difference schemes gives rise to instabilities of different types. However, cellular automats are also quite efficient for solving simpler problems, in particular, for simulations of the spatial structure of a parenchymatous tissue. The algorithm that we realised is described by the sequence of the following steps.

(i) A grid of cells is superimposed on an object. A random number uniformly distributed in the interval from 0 to 1 is assigned to each cell.

(ii) A threshold (in our case, 0.45) is specified that separates all random numbers to the sets of zeroes and units: if a number is smaller than the threshold, 0 is assigned to the cell, otherwise 1 is assigned.

(iii) The vicinity of each cell is considered: if the number of zeroes in the cell vicinity greater, the value 0 is assigned to the cell, otherwise 1 is assigned.

(iv) Step 3 is repeated the required number of times. In our case, the number of iterations was 1000.

Figure 4 shows the spatial structure of an object specified on a triangular grid, which we used to estimate the possibility of detecting tumour inhomogeneities against the background of a random healthy tissue. The parenchymatous component synthesised by using the algorithm described above is shown in grey colour. The values of optical parameters in the models of fat, parenchymatous, and tumour tissues were chosen based on the experimental data obtained by various authors by different methods of measuring the optical properties of biological tissues. Our

analysis of these data has shown that the values of the absorption coefficient μ_a and the reduced scattering coefficient μ_s' measured *in vitro* and *in vivo* are considerably different. Thus, according to *in vitro* data obtained by the inverse Monte-Carlo method [30], the absorption coefficient of a healthy breast tissue is $0.1-0.5\ \mathrm{cm}^{-1}$, while according to *in vivo* DOT [10], this coefficient is between 0.028 and $0.032\ \mathrm{cm}^{-1}$. We used the results of *in vivo* DOT measurements obtained by using both approximate methods of localisation of inhomogeneities with regularisation [8–11] and multistep Newton-like algorithms [31–35] (Table 1). Because we consider in this paper the case of absorbing inhomogeneities, we neglected fluctuations of the reduced scattering coefficient and assumed that its value was the same ($\sim 10\ \mathrm{cm}^{-1}$) for all structures being simulated. Thus, the speed of light in the medium and the diffusion coefficient in our calculations were $0.0214\ \mathrm{cm\ ps}^{-1}$ and 0.034 cm, respectively, and the absorption coefficients of the fat tissue, parenchyma, and tumour were 0.05, 0.06, and $0.075\ \mathrm{cm}^{-1}$, respectively.

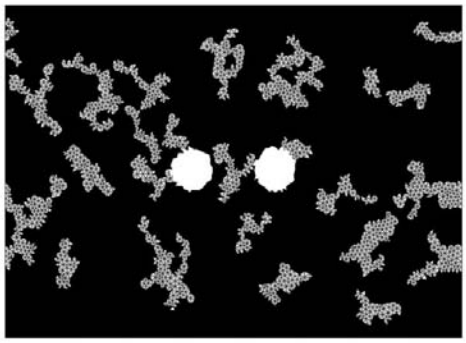

Figure 4. Example of simulation of the spatial structure of a random breast tissue with macroinhomogeneities.

Optical projections were simulated by the finite element method by solving the nonstationary diffusion equation with an instant point source. Time-resolved signals (so-called time point spread functions) were calculated for each source–detector pair as photon fluxes on object boundaries. The positions of sources and detectors are shown in Fig. 1. Optical projections were determined for the delay time $t = 600$ ps from the expression $g(t) = [I_0(t) - I(t)]/I_0(t)$, where $I_0(t)$ is an unperturbed signal calculated for a homogeneous medium and $I(t)$ is a signal perturbed by inhomogeneities. The diffusion tomograms were reconstructed by using the MART on a 137×100 grid described in section 2. The regularised solution was obtained after ten–twenty iterations.

Diffuse tomograms were reconstructed by using a simplified approach in which an image was divided into two regions, each of them containing a circular macroinhomogeneity simulating a tumour. A point spread function corresponding to an individual region was calculated by specifying a point inhomogeneity in a triangle at the centre of a circular inhomogeneity. To obtain the regularised solution, each iteration of the restoration procedure with the steepest descent algorithm [26] was repeated 5–10 times.

The postprocessing of restored images consisted in the successive application of analytic and statistical CFs to them. As the analytic function, power and exponential functions were used. The exponential of the form $C(z) = \exp(B_1 z) + B_2$ was parametrised so that coefficients B_1 and B_2 were determined from the condition of the equality of the volumes of figures restricted by the object

Table 1. Absorption coefficients and reduced scattering coefficients of breast tissues measured by the DOT method [8–11, 31–35].

Tissue type	Measurement regime and method	Inverse problem solution method	Wavelength/nm	μ_a/cm^{-1}	μ_s'/cm^{-1}	References
Healthy tissue Duct carcinoma	TR, TDT	ILLS	785	~ 0.04 0.08–0.12	9.0–10.8 9.0–11.6	[8]
Healthy tissue Carcinoma Fibroadenoma	TR, FDT	ART	830	0.03–0.05 0.07–0.08 0.05–0.06	9.3–11.9 – –	[9]
Healthy tissue Duct carcinoma	TR, TDT	ILRW	670–785	0.028–0.032 0.055–0.08	8.3–9.4 11.5–14.8	[10]
Fatty tissue Parenchyma Cancer tumour	TR, TDT	ILLS	670–785	0.025–0.048 0.032–0.077 0.037–0.063	6.1–14.2 8.4–14.3 11.8–15.0	[11]
Healthy tissue Fibroadenoma	TR, FDT	NR	750	0.03–0.05 0.07–0.09	11–13 9–11	[31]
Healthy tissue Duct carcinoma	TR, FDT	NR	761–826	0.042–0.053 ~ 0.1	10.4–11.6 ~ 15.0	[32]
Healthy tissue Carcinoma	TR, FDT	NR	761–826	0.038–0.065 0.055–0.095	9.8–10.2 14.0–15.1	[33]
Healthy tissue Cancer tumour Fibroadenoma	TR, TDT	NR	780–815	0.035–0.07 0.085–0.1 0.075–0.09	– 7.2–8.5 –	[34]
Healthy tissue Carcinoma Fibroadenoma	TR, TDT	NR	780	0.04–0.07 0.09–0.15 –	6.0–9.5 8.5–11.0 6.0–8.0	[35]

Note. (TR) transmission regime; (TDT) time-domain measurement technique; (ILLS) inhomogeneity localisation with regularisation by the method of least squares; (FDT) frequency-domain measurement technique; (ART) algebraic reconstruction technique; (ILRW) inhomogeneity localisation with regularisation by the random walk method; (NR) Newton–Rafson algorithm.

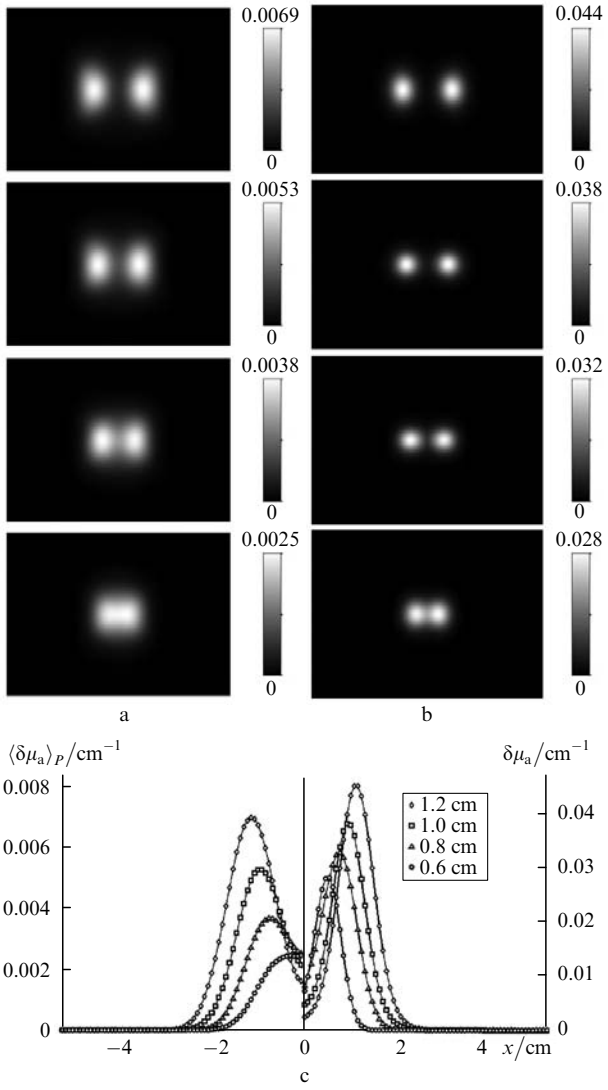

Figure 5. Results of the reconstruction (a) and restoration (b) of four objects for estimating the resolution limit and profiles of reconstructed inhomogeneities (c). The intensity scales of images are graduated in reverse centimetres; the lines of images from top to bottom correspond to inhomogeneity diameters 1.2, 1.0, 0.8, and 0.6 cm.

function $z = \delta\mu_a(x, y)$ before and after postprocessing. The statistical CF was formed automatically according to the algorithm described in section 3.

4.2 Results of simulations and their analysis

Figure 5 presents the results of the reconstruction and space-varying restoration of four objects for estimating the resolution limit. Due to averaging over the spatial distribution of photons, inhomogeneities in all tomograms in Fig. 5a are reproduced in the deformed ('elongated') form. One can see that restoration (Fig. 5b) considerably improves the shape of inhomogeneities and improves the spatial resolution. However, the profiles of inhomogeneities have the characteristic 'Gaussian' shape even after restoration (Fig. 5c) and are far from ideal 'steps' inherent in real images.

The spatial resolution was estimated quantitatively by using the modulation transfer function (MTF) representing the amplitude of the response of a linear spatially invariant system to a harmonic signal and characterising a contrast with which structures with different spatial frequencies are reproduced. Because, as mentioned above, in our case the model of a filter invariant to the spatial displacement cannot be applied in a strict sense, we used the MTF to estimate roughly the resolution limit near the object centre. The modulation transfer coefficient was estimated from the profile of each image in Fig. 5 as the relative depth of a dip between two peaks. The discrete values of the spatial frequency were assigned to diameters of inhomogeneities. The modulation transfer function was constructed by four points as the dependence of the modulation transfer coefficient on the spatial frequency (Fig. 6). One can see from Fig. 6 that structures with frequencies no more than 0.70 and 0.86 cycles cm^{-1} (i.e. of size no less than 0.71 and

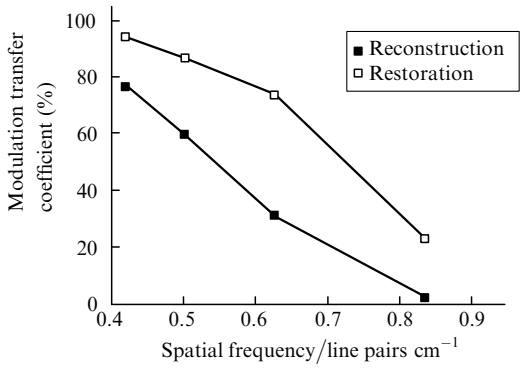

Figure 6. Modulation transfer function constructed by data in Fig. 5.

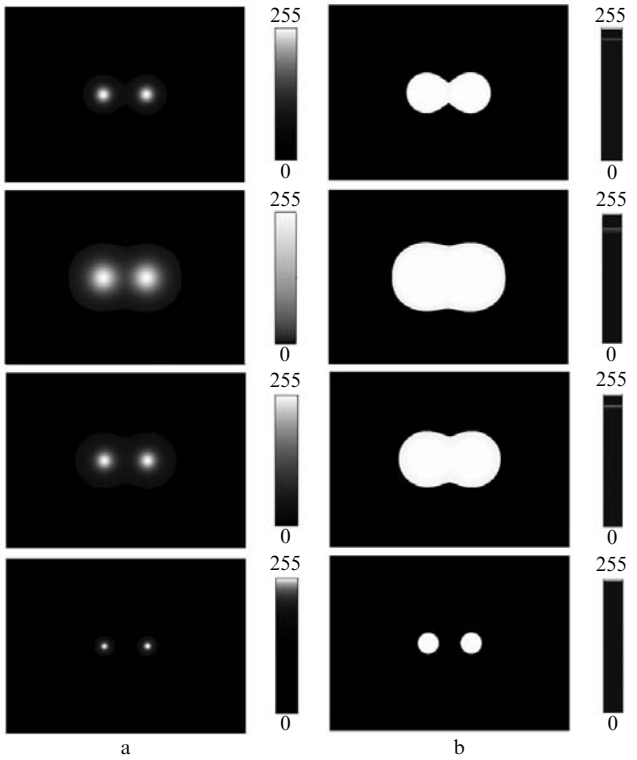

Figure 7. Examples of the action of nonlinear CFs on the restored tomogram visualising inhomogeneities of diameter 1.0 cm; (a) result of the action of analytic CFs (from top to bottom): power function $C(z) = z^2$, power function $C(z) = \sqrt{z}$, exponential $C(z) = \exp(z)$, and parametrised exponential $C(z) = \exp(B_1 z) + B_2$; (b) result of the subsequent application of statistical CFs. The image intensities are normalised.

0.58 cm) will be reconstructed with a contrast of no less than 20 % (the conditional Rayleigh limit of visual resolution [36]) in unprocessed tomograms and tomograms subjected to space-varying restoration, respectively. Although the value 0.58 cm is somewhat worse than the resolution of diffusion tomograms obtained by using Newton-like algorithms, it is quite comparable with it.

Figure 7 presents the examples of action of nonlinear CFs on the restored tomogram visualising inhomogeneities of diameter 1.0 cm. It follows from analysis of Fig. 7 that in the case of 'simple' models (absorbing macroinhomogeneities against the background of a homogeneous scattering medium) it is possible to select a combination of nonlinear CFs providing a complete reconstruction of the real structure of inhomogeneities (Fig. 7b). Note that such an approach based on the formation of nonlinear CFs offers advantages compared to the standard threshold filtration. In the case of the threshold transformation, a part of the image is discarded and is replaced by a background value of the object function. This can lead to the loss of important details in the reconstruction of random structures. Nonlinear CFs are applied to all pixels of the image, which, in the case of properly selected parameters of functions, allows one not only to preserve but efficiently distinguish the informative details of the image.

Figure 8 presents the results of reconstruction, restoration, and nonlinear postprocessing of an object simulating a random medium with macroiinhomogenities presented in Fig. 4. One can see that in the case of a complex model of a random medium, the postprocessing method considered above gives artefacts (the arrow in Fig. 8c), which, however, can be excluded based on *a priori* information contained in reconstructed and restored tomograms. The images in Fig. 8d demonstrate the principal possibility of localisation and determination of the shape of inhomogeneities without the selection of analytic CFs. Note, however, that the visual analysis of the reconstruction results is considerably complicated in this case.

The reconstruction and postprocessing time for one image with the use of a 1.7-GHz Pentium 4, 256-MB RAM Intel PC in the MATLAB medium was less than 1 min, 15 – 20 s being spent for reconstruction and 30 – 40 s for postprocessing. A comparative analysis of the calculation rate presented in [5] has shown that the reconstruction time of a tomogram by using the TOAST (Temporal Optical Absorption and Scattering Tomography) software package [37] realising the Newton – Raphson algorithm is several times longer. Note also that data processing can be further accelerated by using a faster software medium than the MATLAB and optimising the relation between sources and detectors. In particular, our studies [21] have shown that the number of sources for the geometry under study can be reduced from 32 to 16 without the loss of the reconstruction quality.

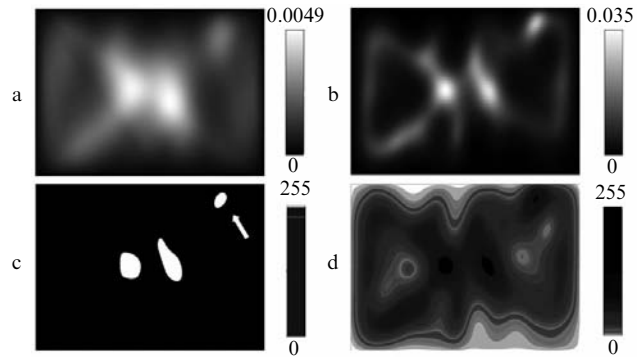

Figure 8. Results of the reconstruction (a), restoration (b), and nonlinear postprocessing of parametrised exponential and statistical CFs (c) and only of statistical CFs (d) with an object simulating a random medium with macroinhomogeneities.

5. Conclusions

We have studied numerically the efficiency of a new realisation of the photon average trajectory method, which is used as an approximate method of diffuse optical tomography for the reconstruction of absorbing macroinhomogeneities of a breast tissue. The realisation includes a single inversion of the system of equations describing a discrete model of reconstruction with the help of a modified multiplicative algebraic technique and postprocessing by using a space-varying restoration and methods for formation of nonlinear colour palettes. The results obtained in the paper show that this method can successfully compete with multistep Newton-like reconstruction techniques, providing comparable reconstruction accuracy and considerably saving the computational time. Of special interest for further studies are the methods of colour interpretation of data, which in the case of simple models provide the perfect reconstruction of inhomogeneities.

Acknowledgements. A.B. Konovalov, V.V. Vlasov, and D.V. Mogilenskikh thank V.M. Kryukov for useful discussions and organisation help. O.V. Kravtsenyuk thanks the European Community and its 6th Mary Curie Program for the support of foreign scientists (Grant No. MIF1-CT-2005-008330).

References

1. Yodh A., Chance B. *Phys. Today*, **48**, 34 (1995).
2. Arridge S.R. *Inverse Problems*, **15**, R41 (1999).
3. Zimnyakov D.A., Tuchin V.V. *Kvantovaya Elektron.*, **32**, 849 (2002) [*Quantum Electron.*, **32**, 849 (2002)].
4. Tuchin V.V. *Lazery i volokonnaya optika v biomditsinskikh issledovaniyakh* (Lasers and Fibre Optics in Biomedical Studies) (Saratov: Saratov State University, 1998).
5. Lyubimov V.V., Kalintsev A.G., Konovalov A.B., Lyamtsev O.V., Kravtsenyuk O.V., Murzin A.G., Golubkina O.V., Mordvinov G.B., Soms L.N., Yavorskaya L.M. *Phys. Med. Biol.*, **47**, 2109 (2002).
6. Lyubimov V.V., Konovalov A.B., Kutuzov I.I., Kravtsenyuk O.V., Kalintsev A.G., Murzin A.G., Golubkina O.V., Soms L.N., Yavorskaya L.M. *Opt. Zh.*, **70**, 37 (2003).
7. Kravtsenyuk O.V., Lyubimov V.V. *Opt. Spektrosk.*, **89**, 119 (2000).
8. Crosenick D., Wabnitz H., Rinneberg H., Moesta K.T., Schlag P.M. *Appl. Opt.*, **38**, 2927 (1999).
9. Niziachristos V., Yodh A.G., Schnall M., Chance B. *Proc. Natl. Acad. Sci. USA*, **97**, 2767 (2000).
10. Chernomordic V., Hattery D.W., Crosenick D., Wabnitz H., Rinneberg H., Moesta K.T., Schlag P.M., Gandjbakhche A. *J. Biomed. Opt.*, **7**, 80 (2002).
11. Crosenick D., Moesta K.T., Wabnitz H., Mucke J., Stroszczynski C., Macdonald R., Schlag P.M., Rinneberg H. *Appl. Opt.*, **42**, 3170 (2003).

12. Gordon R., Bender R., Herman G.T. *J. Theor. Biol.*, **29**, 471 (1970).
13. Nagy J.G., Palmer K., Perrone L. *Numerical Algorithms*, **36**, 73 (2004).
14. Konovalov A.B., Vlasov V.V., Kravtsenyuk O.V., Lyubimov V.V. *EURASIP J. Adv. Sign. Process.*, **2007**, 34747 (2007).
15. Mogilenskikh D.V. *Proc. 10th Intern. Conf. on Computer Graphics and Vision* (Moscow, Russia, 2000) p. 201.
16. Schweiger M., Arridge S.R., Hiraoka M., Delpy D.T. *Med. Phys.*, **22**, 1779 (1995).
17. Arridge S.R., Cope M., Delpy D.T. *Phys. Med. Biol.*, **37**, 1531 (1992).
18. Konovalov A.B., Lyubimov V.V., Kutuzov I.I., Kravtsenyuk O.V., Murzin A.G., Mordvinov G.B., Soms L.N., Yavorskaya L.M. *J. Electron. Imaging*, **12**, 602 (2003).
19. Konovalov A.B., Kiselev A.N., Vlasov V.V. *Pattern Recognition and Image Analysis*, **16**, 249 (2006).
20. Konovalov A.B., Vlasov V.V., Kalintsev A.G., Kravtsenyuk O.V., Lyubimov V.V. *Kvantovaya Elektron.*, **36**, 1048 (2006) [*Quantum Electron.*, **36**, 1048 (2006)].
21. Konovalov A.B., Mogilenskikh D.V., Vlasov V.V., Kiselev A.N., in *Vision Systems: Applications*. Ed. by G. Obinata and A. Dutta (Vienna: I-Tech Education and Publishing, 2007) Ch. 26, p. 487.
22. Fish D.A., Grochmalicki J., Pike E.R. *J. Opt. Soc. Am. A*, **13**, 464 (1996).
23. Konovalov A.B., Vlasov V.V., Uglov A.S., Shelkovenko T.A., Pikuz S.A. *Proc. 2nd Intern. Symposium on Communications, Control and Signal Processing* (Marrakech, Morocco, March 2006, on CD-ROM).
24. Kamm J., Nagy J.G. *Linear Algebra Appl.*, **284**, 177 (1998).
25. Ng M.K., Chan R.H., Tang W.-C. *SIAM J. Sci. Comput.*, **21**, 851 (1999).
26. Kaufman L. *IEEE Trans. Med. Imag.*, **12**, 200 (1993).
27. Pei Y., Lin F-B., Barbour R.L. *Opt. Express*, **5**, 203 (1999).
28. Toffoli T., Margolus N. *Cellular Automata Machines* (London: MIT Press, 1987; Moscow: Mir, 1991).
29. Malinetskii G.G., Stepantsov M.E. *Zh. Vychisl. Mat. Mat. Fiz.*, **36**, 137 (1996).
30. Key H., Davies E.R., Jackson P.C., Wells P.N.T. *Phys. Med. Biol.*, **36**, 579 (1991).
31. McBride T.O., Pogue B.W., Jiang S., Osterberg U.L., Paulsen K.D., Poplack S.P. *Opt. Lett.*, **26**, 822 (2001).
32. McBride T.O., Pogue B.W., Poplack S.P., Soho S., Wells W.A., Jiang S., Osterberg U.L., Paulsen K.D. *J. Biomed. Opt.*, **7**, 72 (2002).
33. Dehghani H., Pogue B.W., Poplack S.P., Paulsen K.D. *Appl. Opt.*, **42**, 135 (2003).
34. Yates T., Hebden J.C., Gibson A., Everdell N., Arridge S.R., Douek M. *Phys. Med. Biol.*, **50**, 2503 (2005).
35. Enfield L.C., Gibson A.P., Everdell N.L., Delpy D., Schweiger M., Arridge S.R., Richardson C., Keshtgar M., Douek M., Hebden J.C. *Appl. Opt.*, **46**, 3628 (2007).
36. Papoulis A. *Systems and Transforms with Applications in Optics* (New York: McGraw-Hill, 1968).
37. Schweiger M., Arridge S.R. http://web4.cs.ucl.ac.uk/research/vis/toast/.